Spherulitic Growth of Coral Skeletons and Synthetic Aragonite: Nature's Three-Dimensional Printing

Chang-Yu Sun,[†,‡] Matthew A. Marcus,[§] Matthew J. Frazier,[†] Anthony J. Giuffre,[†] Tali Mass,[∥] and Pupa U. P. A. Gilbert*[,†,‡,⊥,#,▽]

[†]Department of Physics, [‡]Materials Science Program, [⊥]Department of Chemistry, and [#]Department of Geoscience, University of Wisconsin−Madison, Madison Wisconsin 53706 United States

[§]Advanced Light Source, Lawrence Berkeley National Laboratory, Berkeley, California 94720, United States

[∥]Marine Biology Department, University of Haifa, Mt. Carmel, Haifa 31905, Israel

S *Supporting Information*

ABSTRACT: **Coral skeletons were long assumed to have a spherulitic structure, that is, a radial distribution of acicular aragonite ($CaCO_3$) crystals with their *c*-axes radiating from series of points, termed centers of calcification (CoCs). This assumption was based on morphology alone, not on crystallography. Here we measure the orientation of crystals and nanocrystals and confirm that corals grow their skeletons in bundles of aragonite crystals, with their *c*-axes and long axes oriented radially and at an angle from the CoCs, thus precisely as expected for feather-like or "plumose" spherulites. Furthermore, we find that in both synthetic and coral aragonite spherulites at the nanoscale adjacent crystals have similar but not identical orientations, thus demonstrating by direct observation that even at nanoscale the mechanism of spherulite formation is non-crystallographic branching (NCB), as predicted by theory. Finally, synthetic aragonite spherulites and coral skeletons have similar angle spreads, and angular distances of adjacent crystals, further confirming that coral skeletons are spherulites. This is important because aragonite grows anisotropically, 10 times faster along the *c*-axis than along the *a*-axis direction, and spherulites fill space with crystals growing almost exclusively along the *c*-axis, thus they can fill space faster than any other aragonite growth geometry, and create isotropic materials from anisotropic crystals. Greater space filling rate and isotropic mechanical behavior are key to the skeleton's supporting function and therefore to its evolutionary success. In this sense, spherulitic growth is Nature's 3D printing.**

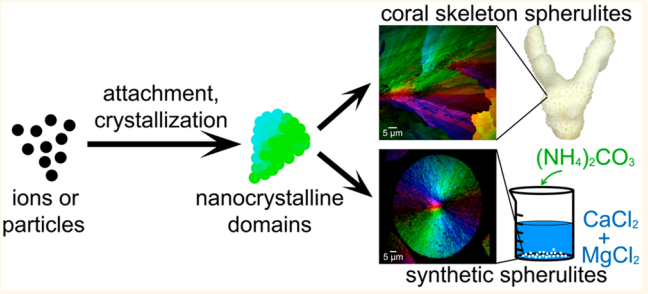

KEYWORDS: *Ion attachment, crystallization by particle attachment, CPA, biomineralization, PEEM, PIC-mapping, mesocrystal*

Spherulites are polycrystalline structures in which acicular crystals radiate from a common center and grow approximately synchronously so the final shape of a spherulite resembles a sphere.[1−7] Figure 1 shows two types of spherulites: "spherical spherulite", in which the crystal fibers start from a point, or "plumose spherulite", in which crystal fibers radiate at an angle from the line.[7]

Spherulites start forming as an aggregate of parallel acicular crystals termed "fibers", then form a "sheaf of wheat" structure, and with the growth of more fibers eventually become complete spheres.[8] In an ideal spherulite, fibers radiate from the center and contain all possible orientations within the sphere. Since the fast-growing axis in aragonite ($CaCO_3$) is the *c*-axis,[9] in spherulites each fiber elongation direction coincides with the crystalline *c*-axis.[10,11] In real spherulites, biogenic[12] and synthetic,[7] the crystal orientations are not perfectly radial nor continuously varying with angle, they deviate slightly from radial and exhibit small but abrupt changes in orientation, termed "branching". In Figure 1 branching angles are smaller than 30° in direction and in crystal lattice orientation. This is distinct from crystallographic branching, which occurs in snowflakes, where crystals have their lattices perfectly co-oriented even when branches grow 60° from one another.

Non-crystallographic branching (NCB) is the first key characteristic of spherulites, distinguishing them from dendritic crystals or other spherical crystal forms.[2,6,7]

Received: January 6, 2017
Accepted: May 31, 2017
Published: May 31, 2017

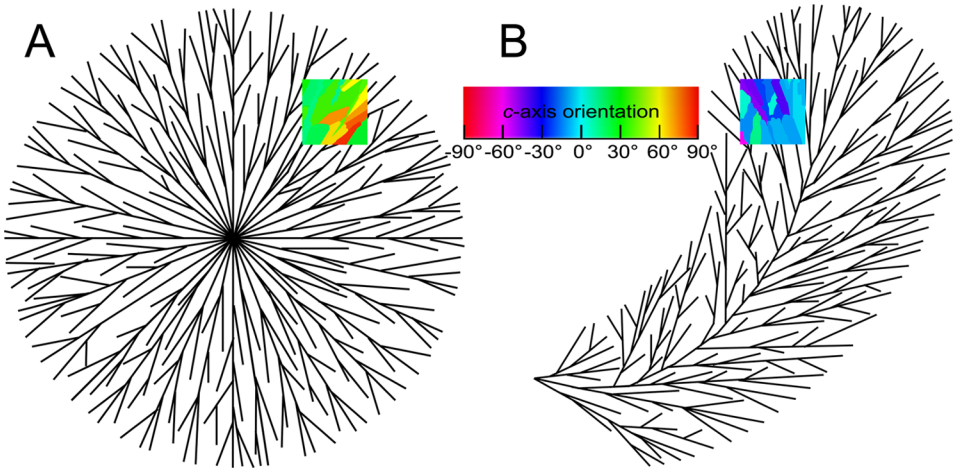

Figure 1. Spherulites can be either (A) spherical or (B) plumose, that is, all crystals fibers radiate from a static point in space, or a point moving along a line, which can be curved. Non-crystallographic branching (NCB) of crystals is shown here as branching angles of less than 30° between crystal fibers. Each line represents both the direction along which a crystal fiber grows and its crystal lattice (*c*-axis) orientation. Each crystal fiber, however, is much wider than each line shows, and abuts all adjacent crystals, such that all together crystal fibers fill the entire volume of a sphere (A) or a curved cylinder (B). The colored insets show two space-filled regions, in which colors indicate different crystal *c*-axis orientations, identifiable in the color legend.

Space-filling is the second key characteristic of spherulites, which distinguishes them from other crystals formed by dendritic or fractal growth.[7,13] To fill space a spherulite must contain crystals oriented in all possible directions, neighboring crystals must be slightly mis-oriented by NCB, therefore the two key characteristics are related to one another.

Aragonite grows acicularly, with growth rate along the *c*-axis 10× greater than along the *a*-axis.[9] Our hypothesis is that the most efficient way for aragonite to fill-space is to grow all crystals along the fast *c*-axis, that is, to grow spherulitically. Space-filling biominerals[14] provide an obvious evolutionary advantage for the organism building them.[10,15]

Crystallization by particle attachment (CPA)[16] is also expected to be faster in that direction because CPA follows the same rules as ion-by-ion attachment from solution, as demonstrated by Gal et al., who showed that *in vitro* CPA forms nanoparticulate calcite rhombohedra.[17] Rodrigues-Navarro also showed this effect.[18] Thus, both aragonite growth by CPA and by ion attachment are faster along the *c*-axis.

Spherulites are found in a wide variety of materials systems, including geologic minerals,[19,20] metal alloys,[21] nonmetallic elements,[5,22] salts,[23,24] organic molecules,[13,25] proteins,[26] and a vast number of synthetic[2,3,27,28] and natural[4] polymers.

Many biominerals have also been described as spherulitic based on their morphologies, including coral skeletons,[10,11,29,30] avian eggshells,[31−33] fish otoliths,[12,34,35] crustacean statoliths,[36] sponges,[37] and kidney stones.[38,39]

The only evidence of spherulites in biominerals obtained from crystal orientation analysis, however, is in bioinduced, kidney stones, which are calcium oxalate monohydrate pathological biominerals.[38,39] Spherulitic growth was suspected to take place in vaterite spicules based on their crystal orientations.[40] Benzerara et al. showed in a *Porites* coral skeleton a radial distribution of aragonite crystal orientations strongly suggestive of spherulitic structure, but did not explicitly conclude that it was spherulitic.[41] For all other biominerals, high resolution, quantitative crystal orientation analysis has not been done. In this study, we do crystal orientation analysis to understand if corals grow their skeletons spherulitically.

Coral skeletons are among the most important biominerals because they form coral reefs, the most biodiverse ecosystems in the ocean. These have received increased attention in recent decades because they are threatened by global warming and ocean acidification.[42,43] Corals that build hard skeletons, also known as stony, or hermatypic, or scleractinian corals, build their skeletons with aragonite today, even though in the past some formed calcite skeletons.[44−46] The centers of calcification (CoCs) are believed to be the nucleation sites for biogenic aragonite in coral. The coral skeleton can be divided into several hierarchical structures: From the CoCs, acicular aragonite fibers grow radially, then arrange into fan-like bundles, and finally group into a structure shaped like a feather duster called "trabecula",[10] similar to that in Figure 1B. "Corallites" are tubular hollow structures on which the polyp sits, with radial plates called "septa", and each septum in cross-section has many CoCs forming a line and crystals radiating from them.

The CoCs were first discovered 120 years ago by Ogilvie[47] and have been studied in depth.[10,48−53] In many different species of coral the CoCs include abundant organic molecules and submicrometer mineral granules.[51,54,55] Although classical assumptions described aragonite fiber growth from the CoC as a purely physicochemical process in which crystals compete for space,[15,29,52] many recent studies have shown that organic molecules are present both within and around the fibers,[54,56] suggesting biologically controlled skeletal formation. Several studies revealed that the fibers consist of nanosized grains.[41,56−58] The observation of nanoparticles is consistent with many other biominerals, such as sea urchin spicules,[17,59] nacre,[60,61] and zebra fish bone,[62] and is considered evidence of crystallization via particle attachment.[16] However, many of the previous studies on coral used only atomic force microscopy (AFM) after etching coral skeletons, thus the size of the particles may have been underestimated, and no orientation information was provided. Information on the nanocrystal orientation is extremely desirable, as it would reveal the arrangement of the coral skeleton building blocks, and thus how aragonite crystals grew.

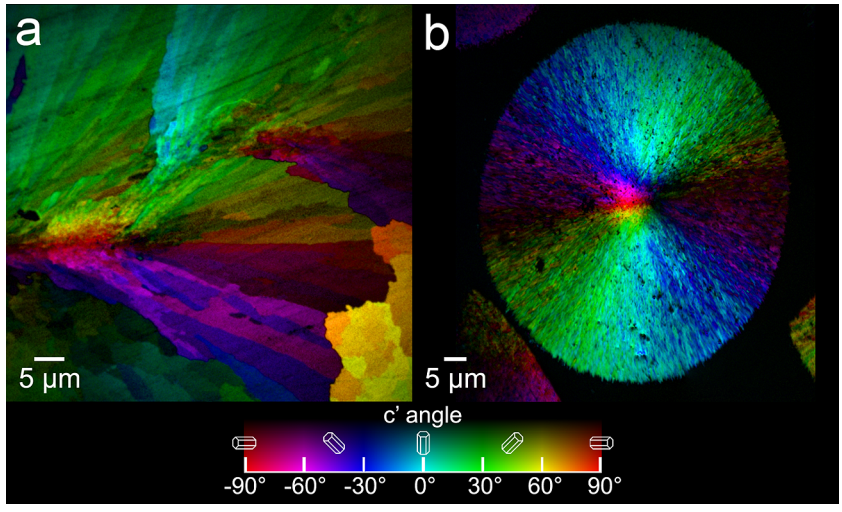

Figure 2. Polarization-dependent imaging contrast (PIC) maps of (a) a coral skeleton and (b) a synthetic aragonite (SA) spherulite. (a) Crystal orientations in coral calcified skeleton from *Stylophora pistillata*. Aragonite crystals radiate as bundles from the CoCs, so that within a bundle adjacent crystals have small angular distances, within 30°, a feature characteristic of spherulitic growth. (b) Crystal orientations in a synthetic spherulite grown in the absence of any organic molecules, observed in cross-section here, which appears to be formed by aragonite fibers. The *c*-axes of aragonite crystals point outward along the radii of a sphere, and therefore display the full spectrum of in-plane orientations in this polished cross-section.

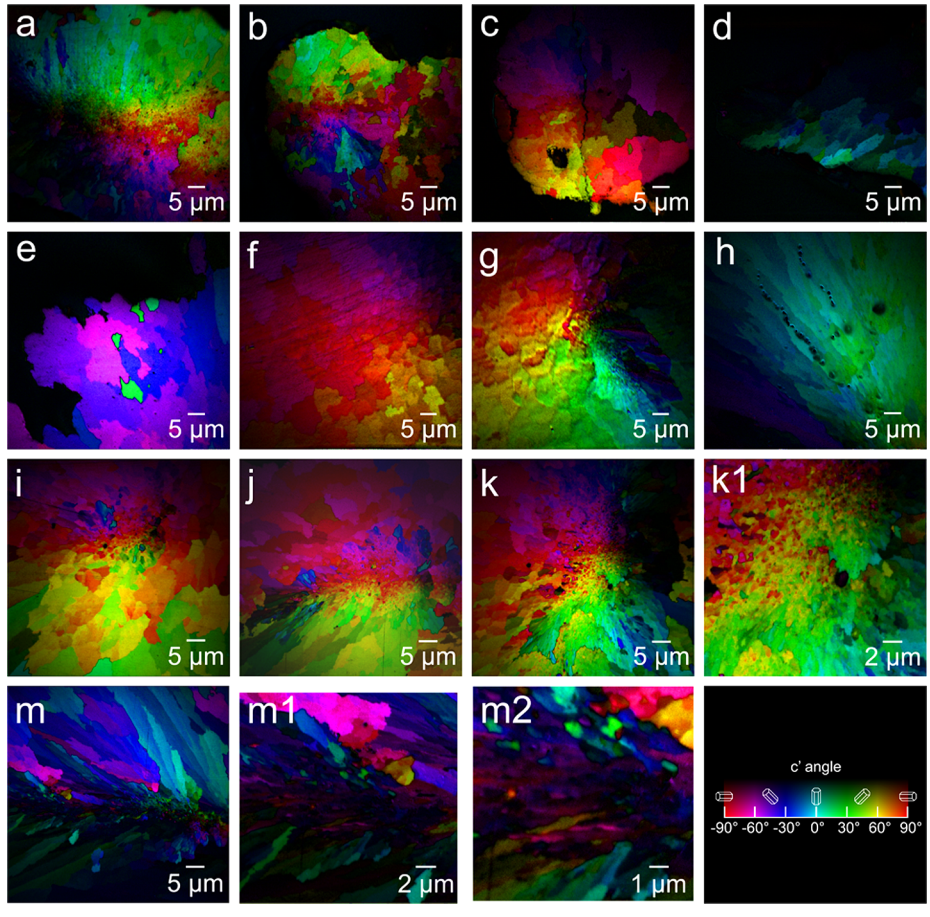

Figure 3. Representative PIC-maps taken in 12 regions from two adult and one spat coral samples. (a) Coral septum in a 4-week old coral spat, after it settled and started calcifying. (b) Region of the same spat skeleton, at the tissue−skeleton interface. The tissue is black, at the top of the images, because it does not contain any crystals. (c−e) Tissue−skeleton interfaces in fresh, forming adult corals. (f) An adult coral skeleton where the polished surface exposed fibers nearly normal to the image plane. (g−m2) CoCs in adult corals. (k1, m1) Zoomed-in PIC-maps (20-μm field-of-view (FoV)) of the regions in panels k and m (60 μm FoV). (m2) Further zoomed-in (10-μm FoV) PIC-map of panel m1. See Figure S2 for more PIC-maps on coral skeleton.

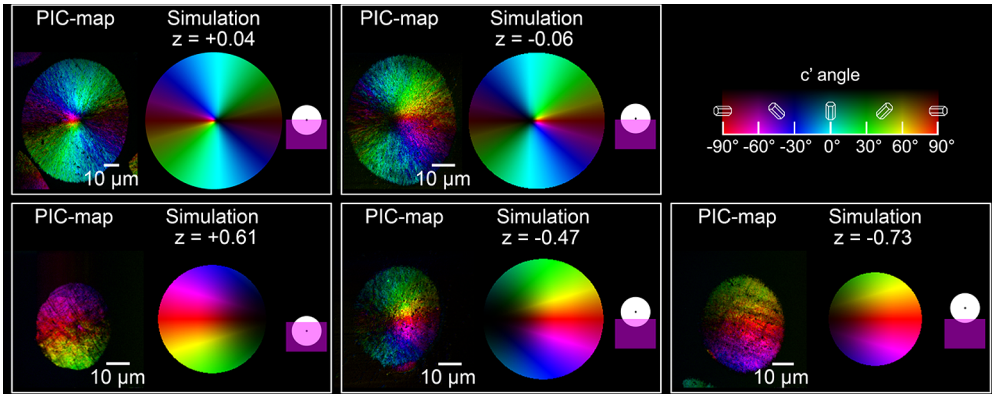

Figure 4. Comparison of experimental PIC-maps of SA spherulites with simulation results, using the same color scheme. Scale bar is 10 μm. For the simulations, we use a simple radial model assuming that spherulites are perfect spheres and all the crystals radiate perfectly along the radii from the centers. The z value is the distance (presented as fraction of radius) from the sample surface to the center of the sphere estimated from the simulations. Positive z means that the center is below the sample surface and the fibers point toward the observer, whereas negative z means that the center was above the surface and was polished off, thus the fibers point away from the observer. Since the X-ray beam illuminates the sample from the right, at a 30° angle from the sample surface, different cross sections of the spherulite result in different c'-axes, and thus result in different color distributions. For example, if the cross-section analyzed is far away from the center and the great circle, such as z = +0.6, cyan would disappear from the PIC-map. The further away from the center, the fewer the colors displayed. From the comparison, we can then select and analyze PIC-maps taken near great circles where c' is the most representative of c. The side-view schematics on the right in each box show the position of the spherulite (white circle, with black dot at the center) with respect to the block of epoxy in which it was embedded (transparent magenta rectangle). The top part of each spherulite is eliminated by polishing. See Figure S3 for more comparisons.

Cohen and McConnaughey showed that crystal morphology depends on crystal growth rate, and that bundles of aragonite crystal fibers that at least morphologically resemble spherulites are likely a result of high growth rates compared to abiotic mineral growth in equilibrium conditions.[10]

Our hypothesis is that spherulitic aragonite fills space faster than any other aragonite structure because the fastest growing direction is the *c*-axis, thus having *c*-axes grow in all possible directions is the most efficient way for polycrystalline aragonite to fill space in three dimensions.

Here we test this hypothesis by analyzing the skeleton of *Stylophora pistillata* coral and synthetic aragonite spherulites for crystal orientations at the nanoscale. *S. pistillata* is abundant in the Indo-Pacific and the Red Sea, and is a commonly used model species for studying coral calcification.[56,63,64] We map the crystal orientations using polarization-dependent imaging contrast (PIC)-mapping, a method based on X-ray linear dichroism in carbonate minerals, which was initially only semiquantitative,[65−69] but is now fully quantitative in providing the *c*-axis orientation of carbonate minerals in three dimensions, expressed with color, including hue and brightness.[40,70,71]

RESULTS AND DISCUSSION

Figure 2a shows a PIC-map of the CoCs in the skeleton of a *Stylophora pistillata* coral. Orientations of the aragonite crystals are color-coded in this map according to their c'-axes, which are the projections of the crystals' *c*-axes onto the polarization plane in a photoemission electron spectromicroscopy (PEEM) experiment.[68,72−75] The color scheme is consistent throughout the article: 0° represents an in-plane, vertical *c*-axis. If the *c*-axis (or its c'-axis projection onto the polarization plane) is rotated clockwise from the vertical the angles vary from 0° to 90°, counterclockwise from 0° to −90°, and the corresponding c' angle hue is assigned to each pixel. The angles formed by the *c*-axes and the polarization plane are represented by brightness, with in-plane *c*-axis pixels displayed in bright colors, and off-plane ones darker, up to black when the off-plane angle is 90°, that is, when the *c*-axis points directly into the X-ray beam.[40,71] The PIC-map in Figure 2a is representative and reproduced in 24 other regions in two adult coral skeletons and one newly settled spat skeleton, presented at various magnifications in Figure 3 and Figure S2. Lower magnification optical micrographs in Figure S1 show the positions in the coral and spherulite samples where the PIC-maps in Figure 2 were taken. Repeated PIC-maps, shown in Figures S2a,b and S2t,u, demonstrate the reproducibility of the method on both the spat and the adult coral skeletons. Aragonite crystal fibers radiate from the CoCs and fill space, leaving no pores between crystals. For comparison and further understanding of crystal orientation and growth mechanisms in coral, we PIC-mapped synthetic aragonite (SA) spherulites grown abiotically, an example of which is presented in Figure 2b.

Additional PIC-maps for coral are presented in Figure 3 and Figure S2, and for SA spherulites in Figure 4 and Figure S3. In Figure 2b, the full spectrum of colors displayed indicates 180° of nearly continuous and radial c'-axis orientations, spanning 360° around the center, because the *c*-axis is a double-headed vector. Note that this cross-section exposes a surface that is close to a center cut through the spherulite, termed great circle. In fact, comparing with simulated PIC-maps as done in Figure 4, we estimate that the surface is only approximately 0.04R away from the center, where R is the radius of the spherulite. This is important because only when the cut is close to the great circle do the crystals lie in plane, and only then the c'-axis is most representative of *c*-axis, as demonstrated in Figure 4 for both experiments and simulations.

Even at a glance, comparing Figure 2 panels a and b reveals some similarity in the color distribution with position and angle with respect to the CoCs or the spherulite center. For example, aragonite crystals pointing in the +30° direction from the CoCs in the coral central bundle, or the center in the synthetic spherulite, both appear green. The same is true at all other observed angles within a coral bundle.

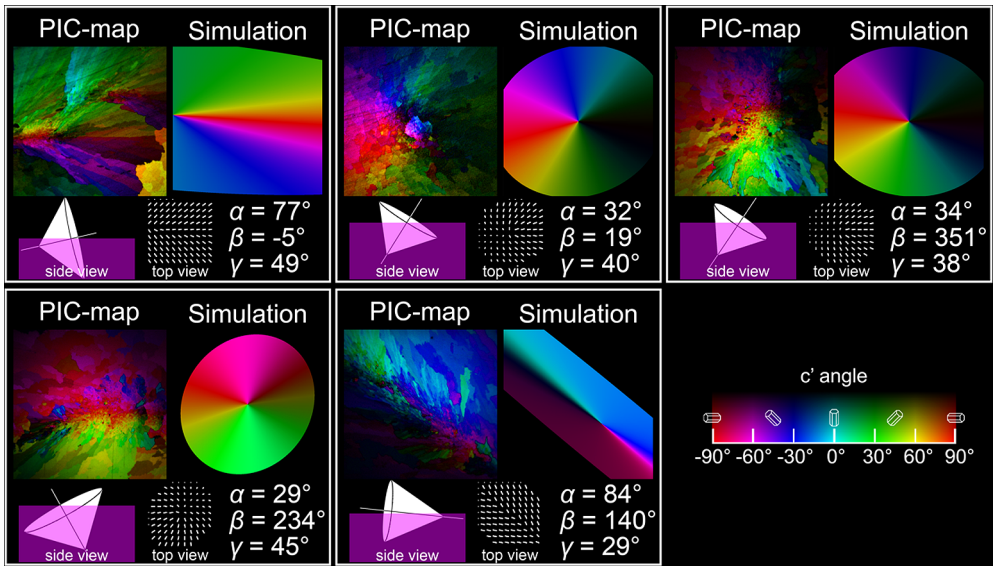

Figure 5. Comparison of selected experimental PIC-maps of coral skeletons (left in each box) with simulation results (right), using the same color scheme. For the simulations, we use an ideal plumose spherulite model, which is an extension of the simple radial model of Figure 4. Here, the nucleus of the radiating crystals is a line instead of a point. The three parameters α, β, and γ are defined in Figure S4. The comparison shows that the colors around the CoCs in the PIC-maps can be matched well with simulation results, thus coral skeletons can be approximated by plumose spherulites. The schematics at the bottom of each box show a side view of the sample, where epoxy is represented by a transparent magenta rectangle, the plumose spherulite central line and a cone of aperture 2γ are shown in white. Along each central line many coaxial cones exist, only one of which is shown for clarity, in a randomly selected position. Again the top part of each plumose spherulite is eliminated by polishing. We also display a top view of an array of *c*-axes obtained from the same simulation. See Figure S5 for more comparisons.

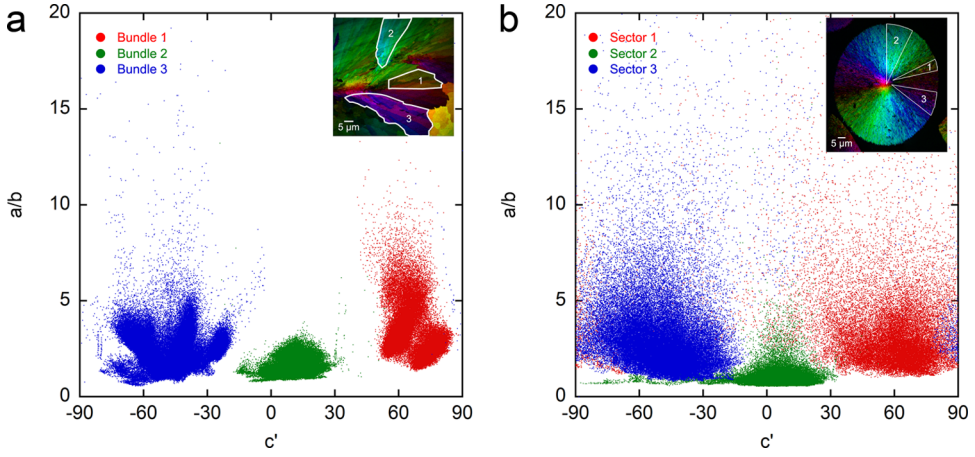

Figure 6. Distribution of crystal orientations in (a) three bundles of coral aragonite crystals from Figure 2a and (b) three circular sectors from the SA spherulite in Figure 2b. The ratio of fit parameters a/b in eq 1 is directly related to the off-plane angle of the crystal *c*-axis, and c' is the in-plane angle. Therefore, the plots here are showing the distribution of *c*-axis orientations in real-space for all the pixels within the correspondingly labeled area. Each bundle in panel a is defined as a set of crystals with similar colors, emanating from the same CoC, elongated in similar directions, with no high-contrast orientation boundaries in the PIC-map, as shown in the inset. For comparison, the sectors in panel b are chosen to have similar sizes and orientations as the bundles in panel a. These plots demonstrate that the angle spread is limited within each coral bundle, as observed in a sector of a spherulite. Figure S6 shows contour maps for these same data.

Figure 4 and Figure S3 show qualitative comparisons of experimental PIC-maps of SA spherulites and simulation results. By assuming an ideal spherulite in a simple radial model where the crystals are radiating from the center, we can reliably simulate the colors of idealized spherulites and compare the simulations with experimental PIC-maps of SA spherulites (see Supporting Information for details on the simulation). Even when the crystals in SA spherulites do not grow perfectly along the radii, the simulation still agrees with experimental data. On the basis of this agreement for spherical spherulites, we expand the simulation to a more complex one for a plumose spherulite as that in Figure 1B. Crystals in a plumose spherulite grow from the central line and radiate outward like cones. The microstructure of a trabecula in coral[1,10,29] resembles a plumose spherulite, in which the CoCs serve as the central line. Simulations of idealized plumose spherulites match the experimentally observed ones in coral skeletons, around the CoCs, as presented in the PIC-maps of Figure 5. Very different distributions of colors are observed across PIC-maps of different coral trabeculae, but it is always possible to match

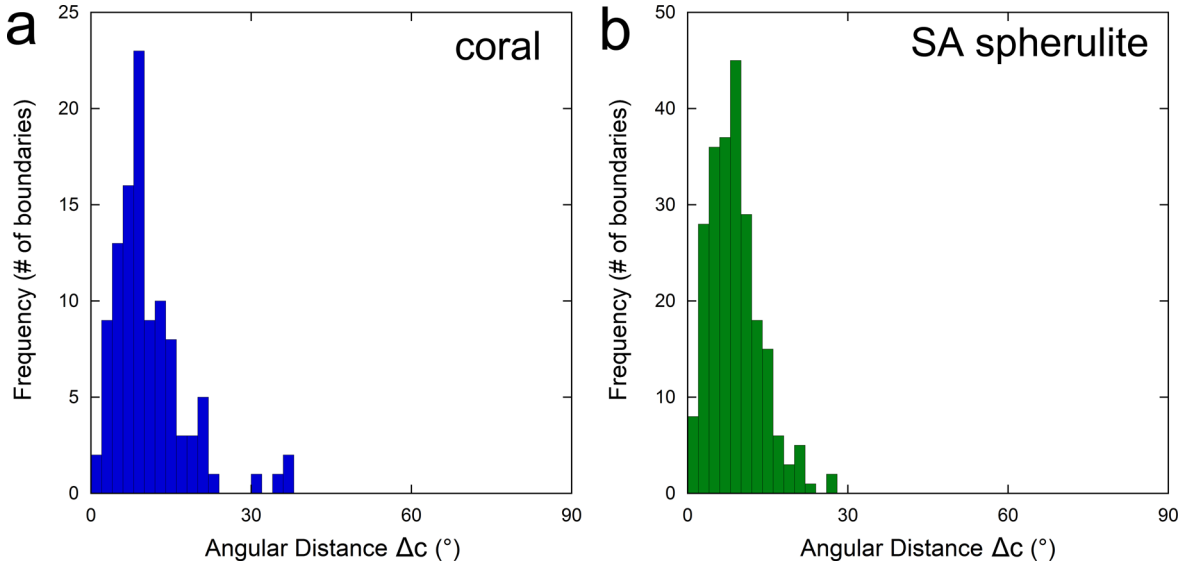

Figure 7. Histogram of angular distances between the *c*-axes of two adjacent crystals in (a) a bundle of crystal fibers in a coral skeleton and (b) an SA spherulite. Two adjacent domains with homogeneous color in PIC-maps were selected and their angular distance Δc, that is, the difference in orientation of their *c*-axes were calculated as described in Figure S8 caption. The crystals for these measurements in coral were within one bundle, not across different bundles, as shown in Figure S8. For the Δc measured here, 102 out of 106 values for coral and the entire 233 values for the SA spherulite fall within the 0°−30° range. Furthermore, both coral and SA spherulite show a peak frequency at $\Delta c \sim$ 10°.

them with analogous simulated plumose spherulites, by best-fitting three parameters: polar angle α, azimuthal angle β, and inclination angle γ, all defined in Figure S4. The excellent agreement between simulated plumose spherulites and experimentally observed coral trabeculae (Figure 5 and Figure S5) demonstrates that crystals around the CoCs grow as plumose spherulites.

To reveal similarities and differences between coral and SA spherulites, we present two different quantitative analyses of the results in PIC-maps, as shown in Figures 6 and 7. The pixel intensity in the set of data used to generate a PIC-map varies as a function of the polarization angle χ according to a cosine-square function[71,76] described by eq 1 in the Methods. Figure 6a shows a plot of fit parameters a/b *versus* c' for all pixels within three *S. pistillata* coral bundles. The highly concentrated data points in the plot illustrate that the crystal orientations are limited within each coral bundle. This indicates that, as the bundle fans out from the CoC, the angle spread within the bundle is not random, but closely matches that of a sector in a complete spherulite, as demonstrated in Figure 6b for comparison. In the plot of Figure 6a all pixels extracted from one bundle are close to one another, as are those in Figure 6b. Furthermore, because the regions selected for coral bundles and SA sectors in Figure 6 have similar positions with respect to the CoC or the center, and span similar angles, the *c*-axis angles are also similar. Blue pixels are mostly between −20° and −70° for c' and between 0.5 and 5 for a/b, green pixels have c' around 0° and a/b below 3, red pixels are mostly between 40° and 80° for c' and between 1 and 6 for a/b. This observation strengthens the idea that coral skeletons grow spherulitically.

Some differences exist between Figure 6 panels a and b. In the SA spherulite sectors there is more scatter in both c' and a/b angles compared to coral bundles, and this is confirmed also in the contour maps of Figure S6. These are 2-dimensional histograms of *c*-axes coordinates for all pixels as in Figure 6. From the contour maps, we can clearly see that the distributions within the similar angle spread range are significantly different for coral and SA spherulites. The explanation for this difference is that a few fibers expand in size as the coral skeleton grows, whereas in SA spherulites fiber sizes remain the same at the center and at the periphery of the spherulite, thus the orientations are many, not a selected few. Indeed, a closer look at the PIC-maps in Figure 2 reveals that the fibers, that is, domains of co-oriented, homogeneously colored pixels, grow larger in size as the bundles fan out from the CoC in the coral trabecula, which does not happen at all in SA spherulites. This may be related to a previous observation: fibers elongate at night and thicken during the day,[56,77,78] thus it is possible that fibers elongate mostly along the *c*-axis at night, and mostly thicken along the *a*- and *b*-axes during the day, but how this is biologically controlled, if it is, remains unknown.

A similar, corroborating result is shown in Figure S7, where we define arc regions at increasing distances from the CoC in one of the coral bundles or the center in a SA spherulite, in order of formation time. The c' angle distributions in Figure S7 demonstrate that initially aragonite grows spherulitically near the CoCs, but as the coral skeleton continues to grow a few crystal orientations prevail and spread into larger domains. This result for the c'-axis in-plane angle in Figure S7 is consistent with that for the full three-dimensional *c*-axis orientations in Figure S6, and with that in PIC-maps from 25 different coral regions in Figure 2, Figure 3, and Figure S2. Whether or not the few prevailing orientations result from active biological control remains unknown.

Next, to understand how domains of co-oriented crystals are oriented with respect to their neighbors we analyzed the angular distance between a domain and its immediate neighbors. The results are presented in Figure 7. The angular distance Δc is a direct measurement of misorientation between the *c*-axes of two adjacent crystals.[40] The histogram in Figure 7a clearly shows that almost all the pairs of adjacent crystals measured have an angular distance between 0°−30°, and the

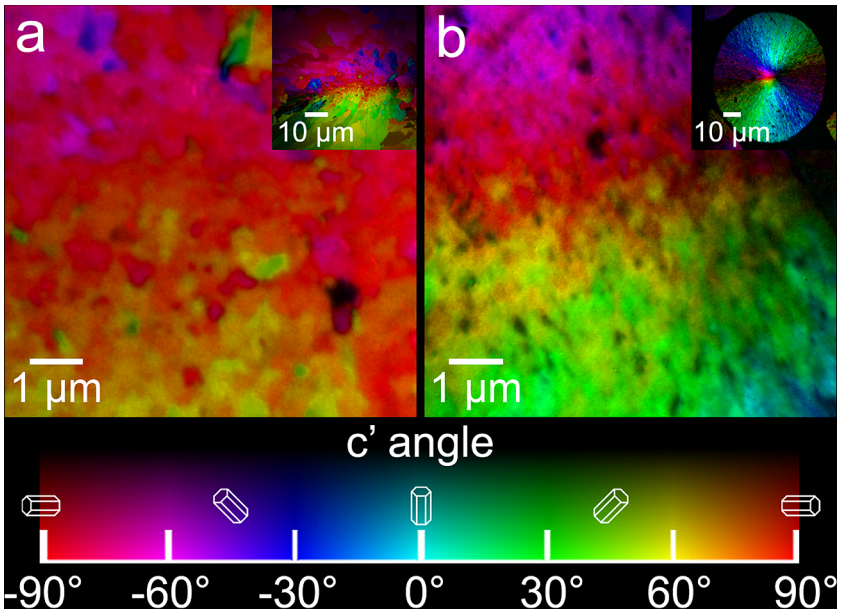

Figure 8. High resolution PIC-maps of (a) coral CoCs and (b) the center of a SA spherulite showing nanoscale domains of crystal orientations. Insets show the lower magnification PIC-maps of the regions from which these zoomed-in PIC-maps with 10 nm pixels were acquired. Both maps show domains of homogeneous orientations (colors), and their adjacent slightly mis-oriented crystal domains with edges jagged at the ~100 nm scale.

most probable angular distance is 10°. This is almost identical to the Δc measurement on an SA spherulite, as plotted in Figure 7b, which also shows a misorientation distribution within 30° and a peak at 10°. This slight misorientation is essential to the formation of spherulites, and is in good agreement with the observations reported across spherulites in various materials systems, including polymers, alloys, minerals, *etc.*[7] Interestingly, even though we found that the crystal fibers in coral become larger at a distance from the CoCs, they exhibit the same Δc profile as the SA spherulite.

In addition to PIC-maps, we also used petrographic microscopy to examine the crystal texture in thin sections of coral skeletons. Figure S9 shows the petrographic micrograph of a *S. pistillata* coral skeleton, polished perpendicular to the CoCs or plumose spherulite central lines, and analyzed in transmission with cross-polarizers in visible light microscopy. Figure S9 clearly shows that there are Maltese crosses everywhere in the coral when the CoC lines run perpendicular to the image plane. Maltese crosses result from cancellation of birefringence every 90°, hence all the vertical or horizontal crystals are black in the image, and dark crosses are observed, with centers indicated by the red arrows in Figure S9. The movie of Figure S9 shows an animated version of this image, acquired as the crossed polarizers were rotated at seven different angles, which makes it much easier to see the Maltese crosses. This is a characteristic of spherulites,[7] and it demonstrates that all 180° in-plane orientations of crystal fibers are present.

From all the crystal orientation analyses in Figures 2−7 and Figures S6−S9, we conclude that *S. pistillata* coral skeletons are indeed spherulitic, as long assumed based on their morphology.

Spherulitic growth is known to take place in growth conditions with high driving forces,[6,79] which are also associated with high growth rates. In biogenic and synthetic aragonite, indeed we see that it enables the crystals to grow along their *c*-axes, which are the fast growing axes (10× faster than along the *a*-axes, whereas along the *b*-axes aragonite only grows 1.6× faster than along the *a*-axes).[9,80] Moreover, the slight misorientation between neighboring crystals driven by spherulitic growth allows them to fill space efficiently. Other growth geometries, such as a radial cluster of needles with fixed needle width, grow crystals fast along the *c*-axes but do not fill space. While aragonite in coral skeletons adopts a spherulitic structure, our data also suggest that its growth is not a purely physicochemical process where crystals simply precipitate from seawater, as conventional coral growth models assumed based on crystal morphology.[15] The change in crystal domain sizes and orientations as trabeculae develop may be associated with passive or active biological control on the growth environment such as pH[11] or the presence of organic molecules.[55]

Previous studies showed that by precisely controlling high supersaturation states, thus high driving forces and high growth rates, along with controlled temperature, it is possible to obtain abiotic spherulitic growth with different polymorphs of $CaCO_3$.[79,81] However, whether these spherulites result from classical ion-by-ion crystal growth from solution or from other crystal growth modes has never been demonstrated. Aggregation of amorphous calcium carbonate (ACC) nanoparticles is a route to achieve high growth rates in $CaCO_3$ systems, and has been reported extensively in calcareous biominerals[59,61,82−84] as a formation mechanism. In a separate study, using spectroscopic analysis, we recently found that *Stylophora pistillata* coral skeletons are formed from ACC precursors (unpublished data).

High resolution PIC-maps were taken at the CoCs of a coral skeleton and at the center of an SA spherulite, as shown in Figure 8. Unexpectedly and interestingly, both of them show subdivision into domains of homogeneous crystal orientation and color at the nanoscale in zoomed-in PIC-maps. These nanodomains, as well as larger domains of orientation, are separated by irregular and jagged edges. Previous studies have shown nanoparticles present in the CoCs of different coral species,[41,54,56] but here we directly measured the crystal orientation at the nanoscale. Figure 8 shows that, instead of

randomly oriented, adjacent crystalline domains are similarly oriented.

The present experimental results show beyond any doubt that the mechanism leading to mis-orientations in spherulites, synthetic or biogenic, is NCB. This confirms theoretical predictions[6] but is not what we expected to find at the nanoscale. We honestly expected to find an aggregate of nanocrystals oriented in all directions, in which only those with *c*-axis orientation close to the radial direction had space to grow and thus prevailed in a competition for space model. What we did find, instead, is that even at the nanoscale, **the orientations are not random but narrowly distributed**, as clearly shown by all PIC-maps and histograms presented here. **The only possible interpretation of this result is NCB at the nanoscale.**

A possible source of NCB is high supersaturation,[7,79,81] which, in the present spherulite growth can be interpreted as greater attachment rate of either individual ions or larger nanoparticles, or greater driving force. Another possible source of NCB is strain at the surface of each nanocrystalline domain or fiber during spherulite growth, which generates slight mis-orientations. Strain can be induced by something minimal, such as the presence of Mg ions in solution.

Spherulitic growth may provide a distinct evolutionary advantage to corals: a full spectrum of crystal orientations explains and contributes to the isotropic mechanical properties reported in coral skeletons,[85] despite the strongly anisotropic nature of aragonite crystals.[9] Furthermore, subdivision into nanoscale components, as observed in Figure 8, is known to increase materials strength and fracture toughness.[86,87]

CONCLUSIONS

With quantitative orientation analyses, and comparing abiotically synthesized aragonite spherulites and biogenic aragonite in *S. pistillata* coral skeletons, we confirm that coral grows spherulitically. Sectors of aragonite spherulites in coral, termed bundles of fibers, fill space and provide the coral skeleton with the needed structural support.

The present data show that adjacent aragonite crystalline domains have slightly different orientations, within 30°, both in SA and in coral skeletons. Interestingly, the size of crystal fibers away from the CoCs is greater in coral skeletons than in SA spherulites.

Corals benefit from spherulitic growth because aragonite growth rates are strongly anisotropic: 10× faster along the *c*-axis direction than along the *a*-axis; thus in spherulites, where most crystal growth is along the fast *c*-axis direction, more efficient space filling is achieved with spherulitic growth than with any other growth geometry. Fast, isotropic, three-dimensional space filling is precisely what 3D printing emulates. Thus, spherulitic growth is Nature's 3D printing, which long predated human-made 3D printing.

METHODS

Materials preparation. Four *Stylophora pistillata* coral skeleton samples were either collected under a special permit from the Israeli Natural Parks Authority in front of the Interuniversity Institute of Marine Biology (IUI) in Eilat (1 old nubbin and fresh spats samples) or cultured in an aquarium system at the Marine and Costal Science Department at Rutgers University (three fresh nubbin samples). Samples of adult coral and spats were prepared with the corallites either in cross-section or longitudinal-section, thus exposing top-views or side views of corallites. The three fresh specimens were fixed in 2% paraformaldehyde and 0.05 M sodium cacodylate buffer in 22 g/L Na_2CO_3, washed with 0.05 M sodium cacodylate buffer in 22 g/L Na_2CO_3, then dehydrated in 50%, 60%, and 70% mixtures of anhydrous ethanol and 1 g/L Na_2CO_3, then in 80% and 90% mixtures of anhydrous ethanol and 0.5 g/L Na_2CO_3, and finally in 100% anhydrous ethanol twice. The duration for each dehydration step was 5 min.

SA formed in the presence of high Mg concentrations often appears in the form of spherulites, especially when preparing a growth solution with 5:1 concentration ratio of Mg^{2+}:Ca^{2+} ions, and diffusing carbonate into it by the spontaneous decomposition and sublimation of solid ammonium carbonate ($(NH_4)_2CO_3$) in the confined air space of a desiccator containing the solution. Other methods, such as solution mixture[8,79] and hydrothermal synthesis,[88] can also produce spherulitic aragonite with different additives and thermal treatments. Aragonite spherulites synthesized from different methods, however, can have different morphologies. For example, the spherulites reported by Koga et al.[88] showed fewer but coarser aragonite rods compared to ours in Figure 2b.

Synthetic aragonite (SA) spherulites were synthesized by diffusing ammonium carbonate ($(NH_4)_2CO_3$) into calcium-containing solutions in a closed container.[89] The solution contained final concentrations of 1 mM $CaCl_2$ and 5 mM $MgCl_2$ to keep the [Mg^{2+}] to [Ca^{2+}] ratio at 5:1. A glass slide of approximately 1 cm × 1 cm area was placed into each beaker along with 10 mL of the mixed solution, and the beaker was then covered with aluminum foil and sealed tightly with Parafilm M (Bemis, Neenah, WI). Three pinholes were pierced through the aluminum foil at the start of the experiment to allow slow diffusion of ammonium carbonate vapor. Ammonium carbonate powder (~10 g) was placed in a separate beaker, sealed and pierced the same way as the growth solution beakers. The solution and the ammonium carbonate were then placed inside a desiccator for 48 h at room temperature. The glass slide on which the spherulites had grown was taken out of the solution, rinsed with ethanol, and air-dried. The spherulites were then scraped off the glass slide using a razor blade to prepare samples for further analyses.

All coral skeleton and SA spherulites samples for PEEM analysis were embedded in EpoFix (EMS, Hatfield, PA), polished with Al_2O_3 suspensions of 300 nm (MicroPolish II, Buehler, Lake Bluff, IL) and then 50 nm (Masterprep, Buehler, Lake Bluff, IL) particle sizes, rinsed with anhydrous ethanol and gently cleaned with TexWipe Cotton (Texwipe, Kernersville, NC), air-dried, and finally coated with 1 nm Pt on the area to be analyzed and 40 nm Pt around it.[68,90] Before polishing the Al_2O_3 suspensions were dialyzed against 22 g/L Na_2CO_3 solution, and the 22 g/L Na_2CO_3 solution was also added onto the polishing felt regularly during polishing.

Polarization-Dependent Imaging Contrast (PIC)-Mapping. PIC-mapping was done by fixing the photon energy at the oxygen K-edge π^* peak (534 eV) and rotating the linear polarization from horizontal to vertical with 5° steps.[70] Nineteen acquired images were then load into a stack and analyzed with GG Macros,[76] which run in Igor Pro (WaveMetrics, Lake Oswego, OR) on both PC and Mac, to produce a quantitative PIC-map. In each pixel the recorded intensity vs polarization angle was extracted, and best fitted by a cosine-square function of the polarization angle χ:

$$f(\chi) = a + b\cos^2(\chi - c') \quad (1)$$

where a, b, and c' are fit parameters. Since the X-ray beam has an incident angle of 30° with respect to the sample surface, c' is the projection of *c*-axis onto the polarization plane. The produced PIC-map then displays c' as the hue and θ' as the brightness for each pixel, where c' is the in-plane angle and θ' is the off-plane angle (with respect to the polarization plane):[40]

$$\theta' = \cos^{-1}\left(\pm\sqrt{(b/a)/(B/A)}\right) \quad (2)$$

B/A is the maximum value of b/a across the image. Thus, the ratio of a and b is directly associated with θ'.

All data for PIC-maps were acquired on PEEM-3 at the Advanced Light Source, LBNL, Berkeley, CA.

PIC-map analyses in Figure 6 and Figures S7–S8 were done by exporting the a, b, and c' maps from Igor Pro and extracting pixel

values with Fiji (ImageJ) 1.51 h from NIH. Each bundle/sector in Figure 6 includes 30 000 to 130 000 pixels.

Angular Distance Calculation. The procedures for calculating the angular distances were as follows: First, domains of homogeneous colors in the PIC-map were selected by hand in Igor Pro. Then, we calculated the fit parameters for that domain as a single crystal.[76] Each domain, or crystal, was then assigned a number, as shown in Figure S9, and the neighboring crystals of that domain were then listed in a table (Table S1 and Table S2). Finally, we calculated the angular distance between each two adjacent crystals by inserting fit parameters a, b, and c' into the equation from Pokroy et al.:[40]

$$\Delta c = \cos^{-1}\left[\frac{1}{D}\left(\sqrt{\frac{b_1 b_2}{a_1 a_2}}\cos(c_1' - c_2') + \sqrt{\left(D - \frac{b_1}{a_1}\right)\left(D - \frac{b_2}{a_2}\right)}\right)\right] \quad (3)$$

All the angular distances calculated were then plotted into the histogram in Figure 7 with a bin size of 2° using Kaleidagraph 4.1 (Synergy Software, Reading, PA).

Thin Section Microscopy. The sample for thin-section petrographic microscopy was first embedded and polished to the cross-section of interest, then glued on one side to a glass slide with a small amount of epoxy resin (EpoFix, EMS, Hatfield, PA), and further polished on the other side. The final thickness of the sample was 15 μm. Petrographic microscopy was done on an Olympus BX51 (Olympus, Center Valley, PA) microscope with white transmission light and cross-polarizers, in Huifang Xu's laboratory, in the Geoscience Department, at UW-Madison.

ASSOCIATED CONTENT

Supporting Information

The Supporting Information is available free of charge on the ACS Publications website at DOI: 10.1021/acsnano.7b00127.

Figures S1−S10 (PDF)

Movie of Figure S9 taken at seven different angles (MOV)

List of the boundaries between neighboring crystals selected in Figure 7a for angular distance calculation (XLSX)

List of the boundaries between neighboring crystals selected in Figure 7b for angular distance calculation (XLSX)

AUTHOR INFORMATION

Corresponding Author

*E-mail: pupa@physics.wisc.edu.

ORCID

Pupa U. P. A. Gilbert: 0000-0002-0139-2099

Notes

The authors declare no competing financial interest.

[▽]Previously publishing as Gelsomina De Stasio.

ACKNOWLEDGMENTS

We thank Elia Beniash for introducing T.M. to P.G.; Paul Falkowski for supplying the corals used for this study; Jonathan Stillman for use of his aquarium facility at UC-Berkeley; Huifang Xu for the use of his petrographic microscope in Geoscience at UW-Madison; Alexander G. Shtukenberg and Alejandro Rodriguez-Navarro for discussions. T.M. acknowledges support from the Israel Science Foundation (Grant 312/15) and from the United States−Israel Binational Science Foundation (BSF-2014035). P.G. acknowledges support from the U.S. Department of Energy, Office of Science, Office of Basic Energy Sciences, Chemical Sciences, Geosciences, and Biosciences Division, under Award DE-FG02-07ER15899, NSF Grant DMR-1603192, and US−Israel Binational Science Foundation Grant BSF-2010065. PEEM experiments were done at the ALS, which is a DOE Office of Science User Facility supported by Grant DE-AC02-05CH11231.

REFERENCES

(1) Bryan, W. H. Spherulites and Allied Structures, Part I. *Proc. R. Soc. Queensl.* **1941**, *LII*, 41−53.

(2) Keith, H. D.; Padden, F. J. A Phenomenological Theory of Spherulitic Crystallization. *J. Appl. Phys.* **1963**, *34*, 2409.

(3) Keith, H. D.; Padden, F. J. Spherulitic Crystallization from the Melt. I. Fractionation and Impurity Segregation and Their Influence on Crystalline Morphology. *J. Appl. Phys.* **1964**, *35*, 1270−1285.

(4) Barham, P. J.; Atkins, E. D. T.; Nieduszynski, I. A. Spherulitic Crystallization in Biopolymers. *Polymer* **1974**, *15*, 762−766.

(5) Bisault, J.; Ryschenkow, G.; Faivre, G. Spherulitic Branching in the Crystallization of Liquid Selenium. *J. Cryst. Growth* **1991**, *110*, 889−909.

(6) Granasy, L.; Pusztai, T.; Tegze, G.; Warren, J. A.; Douglas, J. F. Growth and Form of Spherulites. *Phys. Rev. E: Stat., Nonlinear, Soft Matter Phys.* **2005**, *72*, 011605.

(7) Shtukenberg, A. G.; Punin, Y. O.; Gunn, E.; Kahr, B. Spherulites. *Chem. Rev.* **2012**, *112*, 1805−38.

(8) Sand, K. K.; Rodriguez-Blanco, J.; Makovicky, E.; Benning, L.; Stipp, S. L. S. Crystallization of $CaCO_3$ in Water−alcohol Mixtures: Spherulitic Growth, Polymorph Stabilization, and Morphology Change. *Cryst. Growth Des.* **2012**, *12*, 842−853.

(9) Lin, A.; Meyers, M. A. Growth and Structure in Abalone Shell. *Mater. Sci. Eng., A* **2005**, *390*, 27−41.

(10) Cohen, A. L.; McConnaughey, T. A. Geochemical Perspectives on Coral Mineralization. *Rev. Mineral. Geochem.* **2003**, *54*, 151−187.

(11) Holcomb, M.; Cohen, A. L.; Gabitov, R. I.; Hutter, J. L. Compositional and Morphological Features of Aragonite Precipitated Experimentally from Seawater and Biogenically by Corals. *Geochim. Cosmochim. Acta* **2009**, *73*, 4166−4179.

(12) Addadi, L.; Weiner, S. Control and Design Principles in Biological Mineralization. *Angew. Chem., Int. Ed. Engl.* **1992**, *31* (2), 153−169.

(13) Shtukenberg, A.; Freundenthal, J.; Gunn, E.; Yu, L.; Kahr, B. Glass-Crystal Growth Mode for Testosterone Propionate. *Cryst. Growth Des.* **2011**, *11*, 4458−4462.

(14) Yang, L.; Killian, C. E.; Kunz, M.; Tamura, N.; Gilbert, P. U. P. A. Biomineral Nanoparticles Are Space-Filling. *Nanoscale* **2011**, *3*, 603−609.

(15) Barnes, D. J. Coral Skeletons: An Explanation of Their Growth and Structure. *Science* **1970**, *170*, 1305−1308.

(16) De Yoreo, J. J.; Gilbert, P. U. P. A.; Sommerdijk, N. A. J. M.; Penn, R. L.; Whitelam, S.; Joester, D.; Zhang, H.; Rimer, J. D.; Navrotsky, A.; Banfield, J. F.; Wallace, A. F.; Michel, F. M.; Meldrum, F. C.; Cölfen, H.; Dove, P. M. Crystallization by Particle Attachment in Synthetic, Biogenic, and Geologic Environments. *Science* **2015**, *349*, aaa6760.

(17) Gal, A.; Kahil, K.; Vidavsky, N.; DeVol, R. T.; Gilbert, P. U. P. A.; Fratzl, P.; Weiner, S.; Addadi, L. Particle Accretion Mechanism Underlies Biological Crystal Growth from an Amorphous Precursor Phase. *Adv. Funct. Mater.* **2014**, *24*, 5420−5426.

(18) Rodriguez-Navarro, C.; Burgos Cara, A.; Elert, K.; Putnis, C. V.; Ruiz-Agudo, E. Direct Nanoscale Imaging Reveals the Growth of Calcite Crystals *via* Amorphous Nanoparticles. *Cryst. Growth Des.* **2016**, *16*, 1850−1860.

(19) Peloquin, A. S.; Verpaelst, P.; Ludden, J. N. Spherulitic Rhyolites of the Archean Blake River Group, Canada; Implications for Stratigraphic Correlation and Volcanogenic Massive Sulfide Exploration. *Econ. Geol. Bull. Soc. Econ. Geol.* **1996**, *91*, 343−354.

(20) Fowler, A. D.; Berger, B.; Shore, M.; Jones, M. I.; Ropchan, J. Supercooled Rocks: Development and Significance of Varioles, Spherulites, Dendrites and Spinifex in Archaean Volcanic Rocks, Abitibi Greenstone Belt, Canada. *Precambrian Res.* **2002**, *115*, 311−328.
(21) Geveling, N. N.; Maslenkov, S. B. Solidification of Eutectic Ni-Ni3Ti Alloys. *Met. Sci. Heat Treat.* **1976**, *18*, 755−760.
(22) Miao, B.; North Wood, D. O.; Bian, W.; Fang, K.; Fan, M. H. Structure and Growth of Platelets in Graphite Spherulites in Cast Iron. *J. Mater. Sci.* **1994**, *29*, 255−261.
(23) Harris, J.; Mey, I.; Hajir, M.; Mondeshki, M.; Wolf, S. E. Pseudomorphic Transformation of Amorphous Calcium Carbonate Films Follows Spherulitic Growth Mechanisms and Can Give Rise to Crystal Lattice Tilting. *CrystEngComm* **2015**, *17*, 6831−6837.
(24) Kniep, R.; Simon, P., Fluorapatite-Gelatine-Nanocomposites: Self-Organized Morphogenesis, Real Structure and Relations to Natural Hard Materials. In *Biomineralization 1*; Springer, 2006; pp 73−125.
(25) Beck, R.; Malthe-Sørenssen, D.; Andreassen, J. P. Formation and Ageing of L-Glutamic Acid Spherulites. *Cryst. Res. Technol.* **2010**, *45*, 753−762.
(26) Coleman, J. E.; Allan, B. J.; Vallee, B. L. Protein Spherulites. *Science* **1960**, *131*, 350−352.
(27) Way, J. L.; Atkinson, J. R. Some Studies of Deformation Processes in Fully-Spherulitic Polypropylene. *J. Mater. Sci.* **1971**, *6*, 102−109.
(28) Gatos, K. G.; Minogianni, C.; Galiotis, C. Quantifying Crystalline Fraction Within Polymer Spherulites. *Macromolecules* **2007**, *40*, 786−789.
(29) Bryan, W. H.; Hill, D. Spherulitic Crystallization as a Mechanism of Skeletal Growth in the Hexacorals. *Proc. R. Soc. Queensl.* **1941**, *LII*, 78−91.
(30) Gilis, M.; Meibom, A.; Domart-Coulon, I.; Grauby, O.; Stolarski, J.; Baronnet, A. Biomineralization in Newly Settled Recruits of the Scleractinian Coral *Pocillopora damicornis*. *J. Morphol.* **2014**, *275*, 1349−65.
(31) Nys, Y.; Hincke, M.; Arias, J.; Garcia-Ruiz, J.; Solomon, S. Avian Eggshell Mineralization. *Avian Poult. Biol. Rev.* **1999**.
(32) Nys, Y.; Gautron, J.; Garcia-Ruiz, J. M.; Hincke, M. T. Avian Eggshell Mineralization: Biochemical and Functional Characterization of Matrix Proteins. *C. R. Palevol* **2004**, *3*, 549−562.
(33) Vianey-Liaud, M.; Hirsch, K.; Sahni, A. S.; Sigé, B. Late Cretaceous Peruvian Eggshells and Their Relationships with Laurasian and Eastern Gondwanian Material. *Geobios* **1997**, *30*, 75−90.
(34) Gauldie, R. W. Polymorphic Crystalline Structure of Fish Otoliths. *J. Morphol.* **1993**, *218*, 1−28.
(35) Falini, G.; Fermani, S.; Vanzo, S.; Miletic, M.; Zaffino, G. Influence on the Formation of Aragonite or Vaterite by Otolith Macromolecules. *Eur. J. Inorg. Chem.* **2005**, *2005*, 162−167.
(36) Wittmann, K. J.; Schlacher, T. A.; Ariani, A. P. Structure of Recent and Fossil *Mysid Statoliths* (Crustacea, Mysidacea). *J. Morphol.* **1993**, *215*, 31−49.
(37) Jackson, D. J.; Thiel, V.; Worheide, G. An Evolutionary Fast-Track to Biocalcification. *Geobiology* **2010**, *8*, 191−6.
(38) Sokol, E.; Nigmatulina, E.; Maksimova, N.; Chiglintsev, A. $CaC_2O_4 \cdot H_2O$ Spherulites in Human Kidney Stones. *Eur. J. Mineral.* **2005**, *17*, 285−295.
(39) Al-Atar, U.; Bokov, A. A.; Marshall, D.; Teichman, J. M. H.; Gates, B. D.; Ye, Z.-G.; Branda, N. R. Mechanism of Calcium Oxalate Monohydrate Kidney Stones Formation: Layered Spherulitic Growth. *Chem. Mater.* **2010**, *22*, 1318−1329.
(40) Pokroy, B.; Kabalah-Amitai, L.; Polishchuk, I.; DeVol, R. T.; Blonsky, A. Z.; Sun, C.-Y.; Marcus, M. A.; Scholl, A.; Gilbert, P. U. P. A. Narrowly Distributed Crystal Orientation in Biomineral Vaterite. *Chem. Mater.* **2015**, *27*, 6516−6523.
(41) Benzerara, K.; Menguy, N.; Obst, M.; Stolarski, J.; Mazur, M.; Tylisczak, T.; Brown, G. E., Jr.; Meibom, A. Study of the Crystallographic Architecture of Corals at the Nanoscale by Scanning Transmission X-Ray Microscopy and Transmission Electron Microscopy. *Ultramicroscopy* **2011**, *111*, 1268−1275.
(42) Venn, A. A.; Tambutté, E.; Holcomb, M.; Laurent, J.; Allemand, D.; Tambutté, S. Impact of Seawater Acidification on pH at the Tissue-Skeleton Interface and Calcification in Reef Corals. *Proc. Natl. Acad. Sci. U. S. A.* **2013**, *110*, 1634−1639.
(43) Holcomb, M.; Venn, A. A.; Tambutte, E.; Tambutte, S.; Allemand, D.; Trotter, J.; McCulloch, M. Coral Calcifying Fluid pH Dictates Response to Ocean Acidification. *Sci. Rep.* **2015**, *4*, 5207.
(44) Coronado, I.; Pérez-Huerta, A.; Rodríguez, S. Crystallographic Orientations of Structural Elements in Skeletons of Syringoporicae (Tabulate Corals, Carboniferous): Implications for Biomineralization Processes in Palaeozoic Corals. *Palaeontology* **2015**, *58*, 111−132.
(45) Coronado, I.; Pérez-Huerta, A.; Rodríguez, S. Analogous Biomineralization Processes Between the Fossil Coral *Calceola sandalina* (Rugosa, Devonian) and Other Recent and Fossil Cnidarians. *J. Struct. Biol.* **2016**, *196*, 173−186.
(46) Coronado, I.; Pérez-Huerta, A.; Rodríguez, S. Primary Biogenic Skeletal Structures in Multithecopora (Tabulata, Pennsylvanian). *Palaeogeogr., Palaeoclimatol., Palaeoecol.* **2013**, *386*, 286−299.
(47) Ogilvie, M. M. Microscopic and Systematic Study of Madreporarian Types of Corals. *Philos. Trans. R. Soc., B* **1896**, *187*, 83−345.
(48) Mass, T.; Drake, J. L.; Haramaty, L.; Rosenthal, Y.; Schofield, O. M.; Sherrell, R. M.; Falkowski, P. G. Aragonite Precipitation by "Proto-Polyps" in Coral Cell Cultures. *PLoS One* **2012**, *7*, e35049.
(49) Adkins, J. F.; Boyle, E. A.; Curry, W. B.; Lutringer, A. Stable Isotopes in Deep-Sea Corals and a New Mechanism for "Vital Effects. *Geochim. Cosmochim. Acta* **2003**, *67*, 1129−1143.
(50) Gagnon, A. C.; Adkins, J. F.; Fernandez, D. P.; Robinson, L. F. Sr/Ca and Mg/Ca Vital Effects Correlated with Skeletal Architecture in a Scleractinian Deep-Sea Coral and the Role of Rayleigh Fractionation. *Earth Planet. Sci. Lett.* **2007**, *261*, 280−295.
(51) Cuif, J.-P.; Dauphin, Y. Microstructural and Physico-Chemical Characterization of 'Centers of Calcification'in Septa of Some Recent Scleractinian Corals. *Paläont. Z.* **1998**, *72*, 257−269.
(52) Constantz, B. R. Coral Skeleton Construction: A Physiochemically Dominated Process. *Palaios* **1986**, *1*, 152−157.
(53) Meibom, A.; Cuif, J. P.; Hillion, F.; Constantz, B. R.; Juillet-Leclerc, A.; Dauphin, Y.; Watanabe, T.; Dunbar, R. B. Distribution of Magnesium in Coral Skeleton. *Geophys. Res. Lett.* **2004**, *31*, L23306.
(54) Cuif, J. P.; Dauphin, Y. The Two-Step Mode of Growth in the Scleractinian Coral Skeletons from the Micrometre to the Overall Scale. *J. Struct. Biol.* **2005**, *150*, 319−331.
(55) Cuif, J.-P.; Dauphin, Y.; Doucet, J.; Salome, M.; Susini, J. XANES Mapping of Organic Sulfate in Three Scleractinian Coral Skeletons. *Geochim. Cosmochim. Acta* **2003**, *67*, 75−83.
(56) Mass, T.; Drake, J. L.; Peters, E. C.; Jiang, W.; Falkowski, P. G. Immunolocalization of Skeletal Matrix Proteins in Tissue and Mineral of the Coral *Stylophora pistillata*. *Proc. Natl. Acad. Sci. U. S. A.* **2014**, *111*, 12728−12733.
(57) Vielzeuf, D.; Garrabou, J.; Baronnet, A.; Grauby, O.; Marschal, C. Nano to Macroscale Biomineral Architecture of Red Coral (*Corallium rubrum*). *Am. Mineral.* **2008**, *93*, 1799−1815.
(58) van de Locht, R.; Verch, A.; Saunders, M.; Dissard, D.; Rixen, T.; Moya, A.; Kroger, R. Microstructural Evolution and Nanoscale Crystallography in Scleractinian Coral Spherulites. *J. Struct. Biol.* **2013**, *183*, 57−65.
(59) Gong, Y. U.; Killian, C. E.; Olson, I. C.; Appathurai, N. P.; Amasino, A. L.; Martin, M. C.; Holt, L. J.; Wilt, F. H.; Gilbert, P. U. P. A. Phase Transitions in Biogenic Amorphous Calcium Carbonate. *Proc. Natl. Acad. Sci. U. S. A.* **2012**, *109*, 6088−93.
(60) Oaki, Y.; Imai, H. The Hierarchical Architecture of Nacre and Its Mimetic Material. *Angew. Chem., Int. Ed.* **2005**, *44*, 6571−5.
(61) DeVol, R. T.; Sun, C.-Y.; Marcus, M. A.; Coppersmith, S. N.; Myneni, S. C.; Gilbert, P. U. P. A. Nanoscale Transforming Mineral Phases in Fresh Nacre. *J. Am. Chem. Soc.* **2015**, *137*, 13325−33.
(62) Mahamid, J.; Aichmayer, B.; Shimoni, E.; Ziblat, R.; Li, C.; Siegel, S.; Paris, O.; Fratzl, P.; Weiner, S.; Addadi, L. Mapping

Amorphous Calcium Phosphate Transformation into Crystalline Mineral from the Cell to the Bone in Zebrafish Fin Rays. *Proc. Natl. Acad. Sci. U. S. A.* **2010**, *107*, 6316−21.
(63) Raz-Bahat, M.; Erez, J.; Rinkevich, B. *In Vivo* Light-Microscopic Documentation for Primary Calcification Processes in the Hermatypic Coral *Stylophora pistillata*. *Cell Tissue Res.* **2006**, *325*, 361−8.
(64) Tambutté, E.; Allemand, D.; Zoccola, D.; Meibom, A.; Lotto, S.; Caminiti, N.; Tambutté, S. Observations of the Tissue-Skeleton Interface in the Scleractinian Coral Stylophora pistillata. *Coral Reefs* **2007**, *26*, 517−529.
(65) Metzler, R. A.; Abrecht, M.; Olabisi, R. M.; Ariosa, D.; Johnson, C. J.; Frazer, B. H.; Coppersmith, S. N.; Gilbert, P. U. P. A. Architecture of Columnar Nacre, and Implications for Its Formation Mechanism. *Phys. Rev. Lett.* **2007**, *98*, 268102.
(66) Metzler, R. A.; Zhou, D.; Abrecht, M.; Chiou, J.-W.; Guo, J.; Ariosa, D.; Coppersmith, S. N.; Gilbert, P. U. P. A. Polarization-Dependent Imaging Contrast in Abalone Shells. *Phys. Rev. B: Condens. Matter Mater. Phys.* **2008**, *77*, 064110.
(67) Gilbert, P. U. P. A. Polarization-Dependent Imaging Contrast (PIC) Mapping Reveals Nanocrystal Orientation Patterns in Carbonate Biominerals. *J. Electron Spectrosc. Relat. Phenom.* **2012**, *185*, 395−405.
(68) Gilbert, P. U. P. A., Photoemission Spectromicroscopy for the Biomineralogist. In *Biomineralization Sourcebook, Characterization of Biominerals and Biomimetic Materials*, DiMasi, E., Gower, L. B., Eds.; CRC Press: Boca Raton, FL, 2014; pp 135−151.
(69) Gilbert, P. U. P. A.; Young, A.; Coppersmith, S. N. Measurement of c-axis Angular Orientation in Calcite ($CaCO_3$) Nanocrystals Using X-Ray Absorption Spectroscopy. *Proc. Natl. Acad. Sci. U. S. A.* **2011**, *108*, 11350−11355.
(70) DeVol, R. T.; Metzler, R. A.; Kabalah-Amitai, L.; Pokroy, B.; Politi, Y.; Gal, A.; Addadi, L.; Weiner, S.; Fernandez-Martinez, A.; Demichelis, R.; Gale, J. D.; Ihli, J.; Meldrum, F. C.; Blonsky, A. Z.; Killian, C. E.; Salling, C. B.; Young, A. T.; Marcus, M. A.; Scholl, A.; Doran, A.; Jenkins, C.; Bechtel, H. A.; Gilbert, P. U. P. A. Oxygen Spectroscopy and Polarization-Dependent Imaging Contrast (PIC)-Mapping of Calcium Carbonate Minerals and Biominerals. *J. Phys. Chem. B* **2014**, *118*, 8449−8457.
(71) Gilbert, P. U. P. A.; Bergmann, K. D.; Myers, C. E.; Marcus, M. A.; DeVol, R. T.; Sun, C.-Y.; Blonsky, A. Z.; Zhao, J.; Karan, E. A.; Tamre, E.; Tamura, N.; Giuffre, A. J.; Lemer, S.; Giribet, G.; Eiler, J. M.; Knoll, A. H. Nacre Tablet Thickness Records Formation Temperature in Modern and Fossil Shells. *Earth Planet. Sci. Lett.* **2017**, *460*, 281−292.
(72) Olson, I. C.; Kozdon, R.; Valley, J. W.; Gilbert, P. U. P. A. Mollusk Shell Nacre Ultrastructure Correlates with Environmental Temperature and Pressure. *J. Am. Chem. Soc.* **2012**, *134*, 7351−7358.
(73) Metzler, R. A.; Tribello, G. A.; Parrinello, M.; Gilbert, P. U. P. A. Asprich Peptides Are Occluded in Calcite and Permanently Disorder Biomineral Crystals. *J. Am. Chem. Soc.* **2010**, *132*, 11585−11591.
(74) Killian, C. E.; Metzler, R. A.; Gong, Y. U. T.; Churchill, T. H.; Olson, I. C.; Trubetskoy, V.; Christensen, M. B.; Fournelle, J. H.; De Carlo, F.; Cohen, S.; Mahamid, J.; Wilt, F. H.; Scholl, A.; Young, A.; Doran, A.; Coppersmith, S. N.; Gilbert, P. U. P. A. Self-Sharpening Mechanism of the Sea Urchin Tooth. *Adv. Funct. Mater.* **2011**, *21*, 682−690.
(75) Killian, C. E.; Metzler, R. A.; Gong, Y. T.; Olson, I. C.; Aizenberg, J.; Politi, Y.; Wilt, F. H.; Scholl, A.; Young, A.; Doran, A.; Kunz, M.; Tamura, N.; Coppersmith, S. N.; Gilbert, P. U. P. A. The Mechanism of Calcite Co-Orientation in the Sea Urchin Tooth. *J. Am. Chem. Soc.* **2009**, *131*, 18404−18409.
(76) GG Macros. http://home.physics.wisc.edu/gilbert/software.htm (accessed April 5, 2017).
(77) Gladfeiter, E. Skeletal Development in *Acropora Cervicornis*: I. Patterns of Calcium Carbonate Accretion in the Axial Corallite. *Coral Reefs* **1982**, *1*, 45−51.
(78) Gladfelter, E. H. Skeletal Development in *Acropora Cervicornis*. *Coral Reefs* **1983**, *2*, 91−100.
(79) Andreassen, J.-P.; Beck, R.; Nergaard, M. Biomimetic Type Morphologies of Calcium Carbonate Grown in Absence of Additives. *Faraday Discuss.* **2012**, *159*, 247.
(80) Checa, A. G.; Rodriguez-Navarro, A. B. Self-Organisation of Nacre in the Shells of Pterioida (Bivalvia: Mollusca). *Biomaterials* **2005**, *26*, 1071−1079.
(81) Beck, R.; Andreassen, J.-P. Spherulitic Growth of Calcium Carbonate. *Cryst. Growth Des.* **2010**, *10*, 2934−2947.
(82) Politi, Y.; Arad, T.; Klein, E.; Weiner, S.; Addadi, L. Sea Urchin Spine Calcite Forms *via* a Transient Amorphous Calcium Carbonate Phase. *Science* **2004**, *306*, 1161−1164.
(83) Seto, J.; Ma, Y.; Davis, S. A.; Meldrum, F.; Gourrier, A.; Kim, Y. Y.; Schilde, U.; Sztucki, M.; Burghammer, M.; Maltsev, S.; Jager, C.; Colfen, H. Structure-Property Relationships of a Biological Mesocrystal in the Adult Sea Urchin Spine. *Proc. Natl. Acad. Sci. U. S. A.* **2012**, *109*, 3699−704.
(84) Gal, A.; Weiner, S.; Addadi, L. A Perspective on Underlying Crystal Growth Mechanisms in Biomineralization: Solution Mediated Growth *Versus* Nanosphere Particle Accretion. *CrystEngComm* **2015**, *17*, 2606−2615.
(85) Pasquini, L.; Molinari, A.; Fantazzini, P.; Dauphin, Y.; Cuif, J. P.; Levy, O.; Dubinsky, Z.; Caroselli, E.; Prada, F.; Goffredo, S.; Di Giosia, M.; Reggi, M.; Falini, G. Isotropic Microscale Mechanical Properties of Coral Skeletons. *J. R. Soc., Interface* **2015**, *12*, 20150168.
(86) Gao, H.; Ji, B.; Jager, I. L.; Arzt, E.; Fratzl, P. Materials Become Insensitive to Flaws at Nanoscale: Lessons from Nature. *Proc. Natl. Acad. Sci. U. S. A.* **2003**, *100*, 5597−600.
(87) Wolf, S. E.; Bohm, C. F.; Harris, J.; Demmert, B.; Jacob, D. E.; Mondeshki, M.; Ruiz-Agudo, E.; Rodriguez-Navarro, C. Nonclassical Crystallization *in Vivo* Et *in Vitro* (I): Process-Structure-Property Relationships of Nanogranular Biominerals. *J. Struct. Biol.* **2016**, *196*, 244−259.
(88) Koga, N.; Kasahara, D.; Kimura, T. Aragonite Crystal Growth and Solid-State Aragonite−Calcite Transformation: A Physico−Geometrical Relationship *via* Thermal Dehydration of Included Water. *Cryst. Growth Des.* **2013**, *13*, 2238−2246.
(89) Falini, G.; Albeck, S.; Weiner, S.; Addadi, L. Control of Aragonite or Calcite Polymorphism by Mollusk Shell Macromolecules. *Science* **1996**, *271*, 67.
(90) De Stasio, G.; Frazer, B. H.; Gilbert, B.; Richter, K. L.; Valley, J. W. Compensation of Charging in X-PEEM: A Successful Test on Mineral Inclusions in 4.4Ga Old Zircon. *Ultramicroscopy* **2003**, *98*, 57−62.